11th International Symposium on Turbulence and Shear Flow Phenomena (TSFP11)
Southampton, UK, July 30 to August 2, 2019

DIRECT PARTICLE-FLUID SIMULATION OF KOLMOGOROV-LENGTH-SCALE SIZE ELLIPSOIDAL PARTICLES IN ISOTROPIC DECAYING TURBULENCE

Konstantin Fröhlich
Institute of Aerodynamics
RWTH Aachen University
Wüllnerstr. 5a, 52062 Aachen, Germany
k.froehlich@aia.rwth-aachen.de

Lennart Schneiders
Institute of Aerodynamics
RWTH Aachen University
Wüllnerstr. 5a, 52062 Aachen, Germany
l.schneiders@aia.rwth-aachen.de

Matthias Meinke
Institute of Aerodynamics
RWTH Aachen University
Wüllnerstr. 5a, 52062 Aachen, Germany

JARA Center for Simulation and Data Sciences
RWTH Aachen University
Seffenter Weg 23, 52074 Aachen
m.meinke@aia.rwth-aachen.de

Wolfgang Schröder
Institute of Aerodynamics
RWTH Aachen University
Wüllnerstr. 5a, 52062 Aachen, Germany

JARA Center for Simulation and Data Sciences
RWTH Aachen University
Seffenter Weg 23, 52074 Aachen
office@aia.rwth-aachen.de

ABSTRACT

A suspension of 60,000 ellipsoidal particles with aspect ratios $1/3 \leq \beta \leq 8$ of Kolmogorov-length-scale size in isotropic decaying turbulence is analyzed via direct particle-fluid simulations, where all turbulent scales and all particle scales are fully resolved. A conservative Cartesian cut-cell method is applied and the particle scales are resolved via adaptive mesh refinement. The parameter setup is chosen to study the effects of the particle shape on turbulence modulation and particle dynamics for particles with a relaxation time on the order of the integral time scale. The focus is on rotational particle dynamics. In particular, it is shown that the prolate particles partially follow the local fluid angular velocity and particles in high vorticity regions have a higher instantaneous angular velocity. However, the particle rotation rate of the prolate particles is reduced compared to the angular velocity of the background turbulence. The auto-correlation of particles with a high rotation has a slow decay rate compared to the angular velocity of the fluid experienced by the particles, i.e., the particles have a delayed response due to their inertia.

INTRODUCTION

Pulverized biomass combustion, pollutant transport in the atmosphere, or the deposition of dust in the human respiratory system are three examples for particle-laden turbulent flows which already demonstrate a great diversity. The interaction of numerous scales and a vast parameter space introduced by the particles can be identified as common features. Many applications involve particles of Kolmogorov-length-scale size with complex shape, where it is not clear if the assumption of an isotropic particle shape is valid. In particular, the non-spherical shape introduces a coupling between the translational and the rotational dynamics of the particles due to orientation dependent forces and torques. Particle dynamics in turbulent suspensions are often studied via a Lagrangian point-particle approach where particle surface stresses are not resolved. In the case of ellipsoidal particles, the model equations derived in Jeffery (1922) are adapted for turbulent suspensions which analytically describe the particle dynamics under creeping steady shear flow conditions. Along with details on the ellipsoidal Lagrangian point-particle model, its limitations are discussed in Voth & Soldati (2017), i.e., the particle size should not be considerably larger than the Kolmogorov-length-scale η of the turbulent flow and the particle Reynolds number Re_p should be small. To overcome the latter limitation, several empirical correlations have recently been proposed for orientation dependent drag coefficients in, e.g., Sanjeevi *et al.* (2018); Ouchene *et al.* (2016), but no "standard drag curve" similar to the case of spherical particles (Clift *et al.* (1978)) has yet been established.

A full resolution of all particle and turbulent scales is required to study finite size particles where fluid inertia effects can not be neglected. Such a fully-resolved approach, which is denoted direct particle-fluid simulation (DPFS), has been used to study the turbulence modulation of isotropic turbulence through 45,000 Kolmogorov-length-scale size spherical particles (Schneiders *et al.* (2017)). Moreover, it has been shown that Lagrangian point-particle models yield acceptable results compared to the reference data generated via DFPS (Fröhlich *et al.* (2018*b*)). Ellipsoidal Lagrangian point-particle models without drag correlations, however, can not reproduce the results of DPFS for finite-size ellipsoidal particles (Fröhlich *et al.* (2018*a*)).

In the following, DPFS are performed to study the rotational dynamics of 60,000 Kolmogorov-length-scale size

ellipsoidal particles suspended in isotropic decaying turbulence. Four suspensions with oblate and prolate ellipsoidal particles are investigated, and the particle aspect ratio ranges from $\beta = 1/3$ to 8 with a constant density ratio of 400. The inertia effects discussed by Csanady (1963), i.e., the particles can not follow the fluid due to their higher inertia, are analyzed with respect to the rotational dynamics. Although the parameter space of the current study is considerably different, it can be expected that the particles have a lower rotation rate than the background turbulence as reported in Bellani *et al.* (2012). They investigated experimentally Taylor-microscale size neutrally buoyant particles suspended in forced isotropic turbulence and assigned the reduced particle rotation rate to the large ratio of the rotational particle relaxation time compared to an estimated characteristic time scale of the vorticity. Due to the full resolution of all fluid and particle scales in DPFS, this estimation can now be replaced by an analysis of the effective fluid scales experienced by the particles. Following earlier studies based on Lagrangian point-particle models for spherical particles (Elghobashi & Truesdell (1992); Squires & Eaton (1991)) and slender body theory for fibres (Shin & Koch (2005)), Lagrangian auto-correlations are considered to provide time scales which represent the rotational particle dynamics and the rotation rate of the fluid experienced by the particles.

In the subsequent Sections, the numerical methods for DPFS are recapitulated. After the introduction the flow configuration, the results of the rotational dynamics are presented. Averaged near-particle flow patterns are shown, where the presence of fluid inertia effects are observed which require the full resolution of the particle scales. Finally, the particle rotation rates are reported and Lagrangian auto-correlations are analyzed.

COMPUTATIONAL SETUP

The solution scheme for conservation equations of mass, momentum, and energy is based on a cell-centered finite-volume discretization on hierarchical Cartesian grids. This method has been thoroughly described and validated in Schneiders *et al.* (2016) and references therein. The conservation equations are integrated in time using an explicit five-step predictor-corrector Runge-Kutta method for an efficient fluid-structure coupling. The structural motion is tracked via a level-set method and the interfaces are sharply resolved using cut cells which facilitates a sharp resolution and strictly conserves mass, momentum, and energy. A flux-redistribution technique stabilizes arbitrary small cut cells. The computational requirements for the full resolution of 60,000 particles is mitigated by solution-adaptive refinement. A complete description of the mathematical model for the fluid phase, the solid phase, and their coupling is presented in Schneiders *et al.* (2017).

Based on, e.g., Lucci *et al.* (2010); Elghobashi & Truesdell (1992); Schneiders *et al.* (2017), isotropic decaying turbulence is established in a fully periodic cube with edge length L via an initialization in spectral space using the model energy spectrum

$$E(\kappa) = \left(\frac{3u_0^2}{2}\right)\left(\frac{\kappa}{\kappa_p}^2\right)\exp\left(-\frac{\kappa}{\kappa_p}\right), \qquad (1)$$

with the initial root-mean-square velocity u_0 and the peak wave number $\kappa_p = 8\pi/L$. The initial Taylor-Reynolds number is $Re_\lambda = 79.1$. The particles are injected at $t_i^* = t_i/t_{ref} = 0.28$, when the velocity-derivative converges at approximately -0.5. As in Gao *et al.* (2013), the time t is non-dimensionalized by $t_{ref} = u_0^2/\varepsilon_0$ using the initial dissipation rate ε_0. Further details and validations are provided in Schneiders *et al.* (2016, 2017).

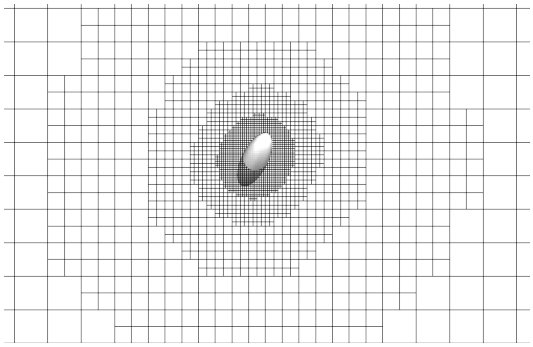

Figure 1. A snapshot of the instantaneous adaptively refined mesh in the vicinity of a prolate particle with aspect ratio 4. The background mesh is sufficient to predict all turbulent scales without turbulence model, and four additional refinement levels are introduced to resolve the particle surface, boundary layers, and wakes. The particles are tracked via a level-set approach and the cut-cell representation of the particle surface is indicated.

Case:	S	P4	P8	O3
β :	1	4	8	$1/3$

Table 1. Particle parameter specifications of the four aspect ratios β for $N = 60{,}000$ particles of the density ratio $\rho_p/\rho = 400$, the volume loading $\phi_v = 0.47 \cdot 10^{-3}$ and the mass loading $\phi_m = 0.19$.

The ambient turbulent scales are resolved via a uniform mesh using 512^3 cells, and four additional refinement levels are introduced in the vicinity of the particles. An illustration of the locally refined mesh is provided in Fig. 1. Due to its complex shape, the prolate particles with aspect ratio 8 represent the computationally most demanding case with about $8 \cdot 10^9$ cells for the full resolution of the particles, whereas the DPFS of the spherical particles requires approx. $5 \cdot 10^9$ cells. The computation is conducted on 48,000 processors, and a dynamic load balancing strategy is applied to substantially improve the parallel efficiency on high performance computers Schneiders *et al.* (2015). The minimum mesh width in the vicinity of the particles is $\Delta x \approx d_p^{vol}/20$ and $\Delta x \lesssim d_p^{min}/10$, with the volume equivalent diameter d_p^{vol} and the diameter of the minor axis d_p^{min} of the particles.

Table 1 shows the four cases which are considered in this study. A suspension of 60,000 particles is analyzed with identical volumetric diameter, density ratio ρ_p/ρ, volume loading ϕ_v, and mass loading ϕ_m. Only the particle aspect ratio β is varied and ranges from $1/3$ through 8. The suspension is dilute and belongs to the two-way coupling regime (Balachandar & Eaton (2010)), i.e., the turbulence can be significantly affected by the presence of the particles, while collisions have minor statistical importance. To avoid the overlapping of the particles, the simple collision

	$t = t_i^*$					$t^* = 2.0$				
Case	d_p^{vol}/η	d_p^{max}/λ	τ_p/τ_ℓ	τ_{rot}/τ_ℓ	τ_{rot}/τ_λ	d_p^{vol}/η	d_p^{max}/λ	τ_p/τ_ℓ	τ_{rot}/τ_ℓ	τ_{rot}/τ_λ
S	1.3	0.09	3.2	0.95	2.8	0.67	0.059	0.83	0.25	0.94
P4	1.3	0.22	2.7	0.81	2.4	0.67	0.15	0.70	0.21	0.76
P8	1.3	0.35	2.2	0.67	1.9	0.67	0.23	0.58	0.17	0.62
O3	1.3	0.13	2.9	0.86	2.5	0.67	0.084	0.74	0.22	0.82

Table 2. Characteristic dimensionless numbers for the four cases at insertion time $t_i^* = 0.28$ and $t^* = 2.0$: ratio of the volume-equivalent particle diameter d_p^{vol} to the Kolmogorov length scale η, ratio of the maximal particle diameter d_p^{max} to the Taylor length scale λ, ratio of the linear particle relaxation time τ_p to the integral time scale τ_ℓ, and ratios of the rotational relaxation time τ_{rot}/τ_ℓ and τ_{rot}/τ_λ with the time scale of the strain-rate fluctuations τ_λ.

model of Glowinski *et al.* (2001) is applied. Some turbulent scales of the flow field, i.e., the Kolmogorov length η, the Taylor length λ, the integral time scale τ_l, and the time scale of the strain-rate fluctuations $\tau_\lambda = \lambda/u'$ with the root-mean-square velocity u' (Tennekes & Lumley (1972)), are related to the particle properties and provided in Table 2 of the injection time t_i^*. The turbulent scales are subject to a continuous change in decaying turbulence and the corresponding values are additionally provided for $t^* = 2.0$. At this time, the rotational particle dynamics are mostly uncorrelated with the injection since the auto-correlation of the particle angular velocity is significantly decreased (not shown here). The volume equivalent diameter d_p^{vol} is on the order of the Kolmogorov length scale η and the maximal diameter of the prolate cases *P*4 and *P*8 is significantly higher. Based on Shapiro & Goldenberg (1993), translational and rotational equivalent relaxation times τ_p and τ_{rot} are used to compute various Stokes numbers, which assume a uniform random particle orientation. The translational equivalent relaxation time is on the order of the integral time scale τ_l and the ellipsoidal particles have a lower Stokes number than spherical particles. Moreover, the aspect ratio has an impact on the equivalent rotational relaxation times τ_{rot} and consequently, the rotational Stokes numbers significantly differ for each case. In total, the equivalent rotational particle relaxation is on the order of the time scale of the strain-rate fluctuations $\tau_\lambda = \lambda/u'$. This particular parameter combination has been chosen to simultaneously study particle dynamics and turbulence modulation for varying particle shape.

RESULTS

The interaction of each particle with the turbulent flow is defined by the ambient flow state. Important quantities such as the particle Reynolds number $Re_p = \rho|\mathbf{U}_p - \mathbf{v}_p|d_p^{vol}/\mu$ with the particle velocity $\mathbf{v}_p$ require an estimation of the ambient fluid velocity $\mathbf{U}_p$. Specifically for the rotational dynamics, the ambient fluid rotation rate $\mathbf{\Omega}_p$ is necessary for the quantification of the time scales experienced by the particles. Therefore, an upwind-biased reconstruction is proposed in Schneiders *et al.* (2019), which will be recapitulated in the subsequent Section using the near-particle flow pattern.

Near-Particle Flow Pattern

Figure 2 shows the local averaged distribution of the near-particle relative fluid velocity $\langle|\mathbf{u}(\mathbf{x}) - \mathbf{v}_p|\rangle$ in a plane which is defined by the force acting upon the particle $\mathbf{F}_p$ and the principal axis of the particle $\widehat{z}$ at $t^* = 2.0$. As an example, the mean velocity field in the vicinity of all particles for the case *P*4, which are inclined by 65 ± 2 degrees, is illustrated. The average particle Reynolds number $Re_p = \rho d_p^{vol}\left|\mathbf{U}_p - \mathbf{v}_p\right|/\mu$ is about $\langle Re_p\rangle = 2.5$, i.e., a stable wake can be expected. It is evident that the force acting on the particle is well aligned with its wake. The length scales η and $\lambda/2$ are provided as a reference. Additionally, Figure 2 illustrates a procedure to estimate the ambient fluid property $\mathbf{U}_p$ via

$$\mathbf{U}_p = \left(\int \mathscr{C}_p^{up}(\mathbf{x})dV\right)^{-1} \int \mathscr{C}_p^{up}(\mathbf{x})\mathbf{u}(\mathbf{x})dV, \qquad (2)$$

where the first term normalizes the upwind-biased weights $w(\mathbf{x})$

$$\mathscr{C}_p^{up}(\mathbf{x}) = \begin{cases} w(\mathbf{x}), & \text{if } \measuredangle(\mathbf{n}_p, \mathbf{F}_p) < \theta_{up} \\ 0, & \text{otherwise} \end{cases} \qquad (3)$$

defined by a Gaussian function

$$w(\mathbf{x}) = exp\{-0.5(\delta_p(\mathbf{x}) - \delta_0)^2/\sigma^2\}. \qquad (4)$$

That is, the local fluid velocity $\mathbf{u}(\mathbf{x})$ is used to estimate the ambient fluid velocity of the particle $\mathbf{U}_p$, if the angle between the normal vector $\mathbf{n}_p$ of the particle surface point closest to $\mathbf{x}$ and the force acting on the particle $\measuredangle(\mathbf{n}_p, \mathbf{F}_p)$ is within the region limited by a predefined angle θ_{up}. The weighting region is further limited by a minimum and maximum distance D_0 and D_1, which define the peak of the Gaussian function $\delta_0 = (D_0 + D_1)/2$. The standard deviation of the Gaussian function is chosen $\sigma = (D_1 - D_0)/6$ such that the weights decrease to 0 if the local distance $\delta_p(\mathbf{x})$ approaches D_1 or D_0. The weighting procedure is fully defined by the parameters D_0, D_1, and θ_{up}. Preliminary results have shown that the thickness of the weighting function has a minor impact on the results. Therefore, the maximum distance is chosen $D_1 = D_0 + d_p^{vol}$ throughout this study. If the weighting region is to close to the particle, the estimation of U_p is disturbed by the particle boundary layer. For large values of D_0, however, filtering effects can be observed and the absolute value of $\mathbf{U}_p$ systematically decreases. An optimal value of D_0 and θ_{up}

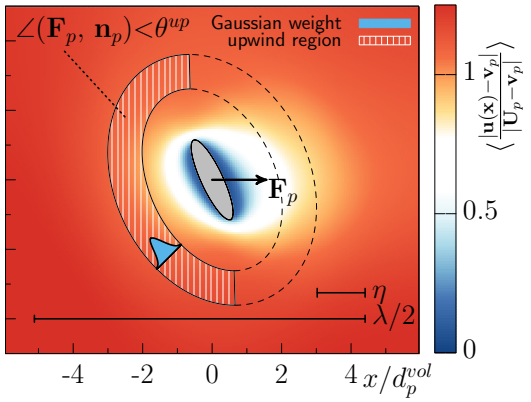

Figure 2. Averaged absolute local near-particle relative fluid velocity of the particles in case P4 inclined by 65 ± 2 degrees at $t^* = 2.0$. The reconstruction of the ambient fluid velocity $\mathbf{U}_p$ and the ambient fluid angular velocity $\mathbf{\Omega}_p$ is illustrated. The shaded area represents the upwind region of Eq. 3 for $\theta_{up} = 0.0$ and the Gaussian weights are described by Eq. 4 with $\delta_0 = (D_0 + D_1)/2 = 2d_p^{vol}$ and $\sigma = d_p^{vol}/6$. The Kolmogorov length scale η and the Taylor length scale λ at $t^* = 2.0$ are included.

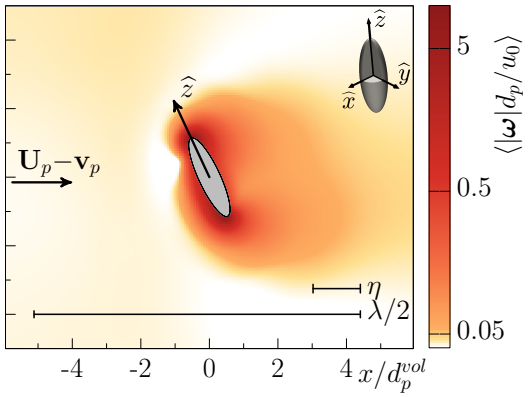

Figure 3. Averaged absolute local near-particle angular fluid velocity of the particles in case P4 inclined by 65 ± 2 degrees at $t^* = 2.0$ normalized by the volume-equivalent diameter d_p^{vol} and the initial root-mean-square velocity u_0. An illustration shows the particle principal axes $\hat{x}$, $\hat{y}$, and $\hat{z}$. The Kolmogorov length scale η and the Taylor length scale λ at $t^* = 2.0$ are included.

is likely to depend on the ambient turbulence, the particle size and shape, and the particle orientation. Therefore, all the results are presented for six different specifications with $D_0 = \{1.5d_p^{vol}, 2.5d_p^{vol}\}$ and $\theta_{up} = \{-0.5, 0.0, 0.5\}$ whenever this is possible. Figure 2 shows the upwind region for $D_0 = 1.5d_p^{vol}$ and $\theta_{up} = 0.0$. Clearly, a majority of the disturbance, including the particle wake and boundary layer, of the particle are avoided by the weighting region. The ambient angular fluid velocity $\mathbf{\Omega}_p$ is reconstructed similarly.

Figure 3 shows the value of the local angular fluid velocity $|\boldsymbol{\omega}| = |1/2 \text{ curl } \mathbf{u}(\mathbf{x})|$ averaged for all particles inclined by 65 ± 2 degrees. As in Fig. 2, effects due to finite fluid inertia can be observed. Note that the vorticity distribution is not symmetric. The particle scales are significantly smaller than the surrounding turbulent scales. Consequently, the vorticity in the vicinity of the particle is about two orders of magnitude higher in vicinity of the particle, and a logarithmic scale has been used for the visualization. High vorticity can be observed in the boundary layer, especially near highly curved surfaces, and in the particle wake. In the upwind regions, lower vorticity can be identified due to an enhanced strain rate. Note that the chosen upwind region for the estimation of the ambient fluid properties defined in Fig. 2 mostly avoids regions with extremely high local fluid vorticity.

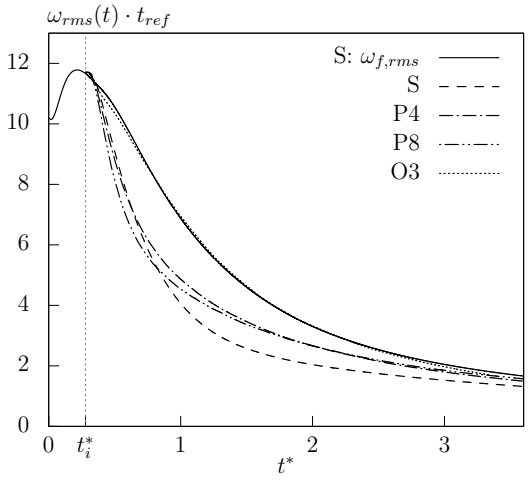

Figure 4. Temporal development of the root-mean-square value of the particle angular velocity ω_{rms} and of the background fluid angular velocity $\omega_{f,rms}$ of case S non-dimensionalized by the reference time $t_{ref} = u_0^2/\varepsilon_0$.

Rotational Particle Dynamics

The root-mean-square value of the particle angular velocity ω_{rms} is depicted in Fig. 4 for the four cases. As a reference, the root-mean-square value of the background fluid angular velocity of case S is included. That is, for the estimation of the background angular velocity of the turbulent flow field, the enhanced fluid angular velocity in the vicinity of the particles is excluded. A threshold distance of $2d_p^{vol}$ measured from the particle surface is chosen and any fluid property within this region is excluded to estimate the background fluid properties. After insertion of the particles at t_i^* with the local angular fluid velocity, the rotation rate of the prolate particles and the spherical particles rapidly decreases. Until $t^* \approx 3.4$, oblate particles have a higher angular velocity. It can be expected that several effects with a complex non-linear interplay ultimately lead to highly shape-dependent particle rotation rates. The rotational dynamics can be classified in spinning and tumbling motion Voth & Soldati (2017), which have their individual rotational relaxation times, and relative angular velocity as well as the strain rate experienced by the particles have an impact on the rotation rates. As in Shin & Koch (2005), filtering effects are expected due to the finite size of the particles especially for case P8. Specifically for case O3, the major axes of the particles are preferentially perpendicular to the direction of the relative velocity $\mathbf{U}_p - \mathbf{v}_p$. A complete report on these effects is beyond the scope of this contribution. Instead, this study focuses on the reduced rotation rates of the prolate particles which consistently have been reported in Bellani *et al.* (2012). One of their possible explanations for the low rotation rate was a delayed response

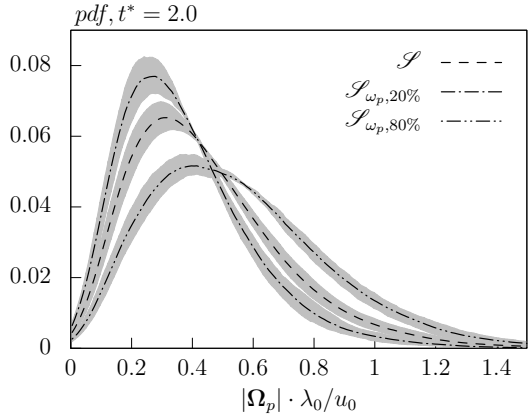

Figure 5. Probability density function (pdf) of the ambient angular velocity at the particle position $|\mathbf{\Omega}_p|$ for three sets of particles at $t^* = 2.0$ of case P4. $\mathscr{S}$ contains all particles which temporarily do not collide, $\mathscr{S}_{\omega_p,20\%} \subset \mathscr{S}$ represents about 20% particles with a low rotation rate, and $\mathscr{S}_{\omega_p,80\%} \subset \mathscr{S}$ represents about 20% particles with the highest rotation rate. The shaded area represents the variation due to various configuration of the reconstruction procedure described by Eq. 2.

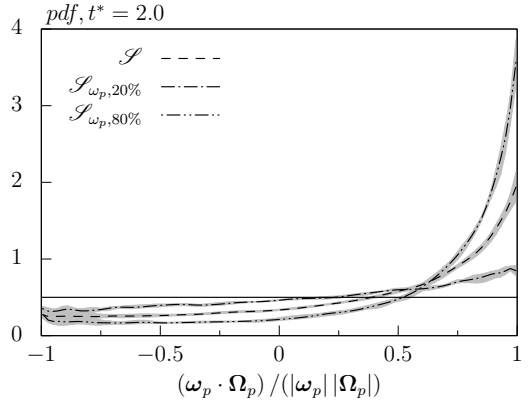

Figure 6. Probability density function of the cosine between the particle rotation rate and the fluid rotation rate at $t^* = 2.0$ for case P4. For a description of the shaded area and the analyzed sets, see Fig. 5.

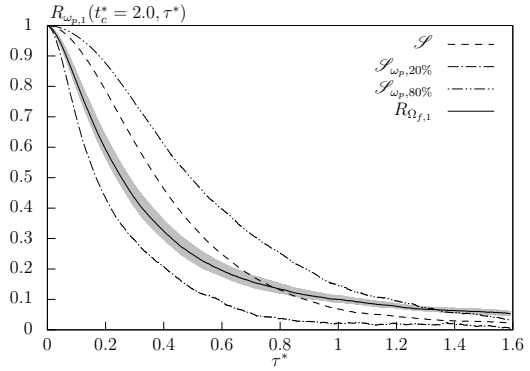

Figure 7. Lagrangian auto-correlation of the first component of the particle angular velocity $\omega_{p,1}$ and the Lagrangian auto-correlation $R_{\Omega_{f,1}}$ of the first component of the ambient fluid angular velocity experienced by the particles of the set $\mathscr{S}$ for case P4 . For a description of the shaded area and the analyzed sets, see Fig. 5.

of the particles on the fluid vorticity due to the particle inertia. Exemplarily, the delayed response of the rotation rate will be examined for the case P4, while the same trend with varying intensity can be observed for the other cases.

Three sets of particles are considered in the following. The set $\mathscr{S}$ consists of all particles which are temporarily not significantly influenced by the presence of any particles in the vicinity, i.e., all particles subject to the collision model are excluded for the statistics. A subset $\mathscr{S}_{\omega_p,20\%} \subset \mathscr{S}$ contains about 12,000 particles with the lowest absolute angular velocity and a further subset $\mathscr{S}_{\omega_p,80\%} \subset \mathscr{S}$ contains about 12,000 particles with the highest absolute angular velocity. The statistics are conducted at $t^* = 2.0$, when the particle rotation rate is not significantly correlated with the initial rotation rate.

Figure 5 shows the probability density function (pdf) of the absolute value of the ambient angular velocity at the particle position $|\mathbf{\Omega}_p|$ normalized by the initial time scale of the strain rate fluctuations λ_0/u_0 for the three sets of particles. As described in the previous Section, six specifications for the estimation of the ambient angular velocity have been applied, and the grey shaded areas represent the variation due to the chosen procedure. Vorticity fluctuations of the size of the particle in the ambient turbulent flow field are differently captured by the estimation procedure such that they are partially filtered. Nevertheless, the three sets of particles clearly experience different local vorticity. Particles in the subset $\mathscr{S}_{\omega_p,80\%}$ are located in regions with high vorticity and particles in the subset $\mathscr{S}_{\omega_p,20\%}$ experience lower vorticity. Indications on preferential concentration could, however, not be detected for all particles $\mathscr{S}$.

To analyze the alignment of the particle rotation rate $\boldsymbol{\omega}_p$ and the ambient fluid rotation rate $\mathbf{\Omega}_p$, the cosine between the rotation rates is considered in Fig. 6. As in Fig. 5, the grey shading illustrates the deviations between the different estimations of $\mathbf{\Omega}_p$. The value 0.5 represents a random uniform distribution, and is included in the figure. It can be observed, that most of the particles $\mathscr{S}$ are preferentially aligned with the ambient fluid rotation of the turbulence $\mathbf{\Omega}_p$. The alignment is significantly higher for the subset $\mathscr{S}_{\omega_p,80\%}$, and consistently lower for the subset $\mathscr{S}_{\omega_p,20\%}$. It follows that the particle rotation rate is substantially affected by the local fluid rotation rate for prolate particles with the chosen Stokes numbers. If the particles encounter regions with high fluid vorticity, the angular velocity of the particles is increased and vice versa. The alignment is, however, perturbed due to the particle inertia which is considered next via auto-correlations.

The Lagrangian auto-correlation for the value ϕ is defined

$$R_\phi(t_c^*, \tau^*) = \frac{\langle \phi(t_c^*) \phi(t_c^* + \tau^*) \rangle}{\langle \phi(t_c^*)^2 \rangle^{1/2} \langle \phi(t_c^* + \tau^*)^2 \rangle^{1/2}}, \qquad (5)$$

where $t_c^* = 2.0$ denotes the initial time to compute the auto-correlation. The corresponding auto-correlations for the particles in the sets $\mathscr{S}$, $\mathscr{S}_{\omega_p,20\%}$, $\mathscr{S}_{\omega_p,80\%}$ are tracked as a function of time. Figure 7 shows the resulting auto-correlations for the first component of the particle rotation rate vector $R_{\omega_{p,1}}$ for the three sets. The particles with an initially high rotation rate $\mathscr{S}_{\omega_p,80\%}$ correlate much longer with their initial value compared to particles with an initially low

rotation rate $\mathscr{S}_{\omega_p,20\%}$. Additionally, the auto-correlation of the first component of the ambient fluid rotation $R_{\Omega_{f,1}}$ is included in Fig. 7 for all particles $\mathscr{S}$. The corresponding results of $R_{\Omega_{f,1}}$ for the subsets $\mathscr{S}_{\omega_p,20\%}$ and $\mathscr{S}_{\omega_p,80\%}$ are similar. $R_{\Omega_{f,1}}$ decays faster than the auto-correlation of the particle rotation rate for all particles in $\mathscr{S}$. This trend is clearly more pronounced for the subset $\mathscr{S}_{\omega_p,80\%}$.
During the time interval in which the auto-correlation is computed, some particles experience collisions and a collision may alter the trajectory of a particle significantly. Therefore, a similar analysis has been conducted, where all particles which have experienced a collision are excluded from the auto-correlations. No significant changes can be observed and the results are quite similar to the distributions shown in Fig. 7.

CONCLUSION AND OUTLOOK

Highly resolved simulations of ellipsoidal particles suspended in isotropic decaying turbulence are conducted and particle shape effects on rotational dynamics have been analyzed. The particles are of Kolmogorov-length-scale size and the particle relaxation time is similar as the integral time scale. About 60,000 particles are required to have a considerable mass and volume loading for two-way coupling effects. Even for moderate mean particle Reynolds numbers $\langle Re_p \rangle \lesssim 3$, pronounced fluid inertia effects can be observed. The rotation rate of the particles is significantly affected by vorticity of the background turbulence. However, the particle rotation rate is reduced due to their inertia and, consequently, their delayed response to the fluid rotation rate seen by the particles.
The analysis of the presented simulations will be extended in a future contribution with an analysis of the shape effects on turbulence modulation and further results on the rotational particle dynamics. Tumbling and spinning motion of the particles will be analyzed and the presented analysis will be extended for each individual rotational component of the particles. Further studies are planned to validate existing drag correlation laws for non-spherical particles. If necessary, new drag correlations, which can predict the results of the DPFS, are to be developed.

ACKNOWLEDGMENT

This work has been financed by the German Research Foundation (DFG) within the framework of the SFB/Transregio Oxyflame (subproject B2). The sup- port is gratefully acknowledged. Computing resources were provided by the High Performance Computing Center Stuttgart (HLRS) and by the Jülich Supercomputing Center (JSC) within a Large-Scale Project of the Gauss Center for Supercomputing (GCS).

REFERENCES

Balachandar, S. & Eaton, J. K. 2010 Turbulent dispersed multiphase flow. *Annu. Rev. Fluid Mech.* **42**, 111–133.

Bellani, G., Byron, M. L., Collignon, A. G., Meyer, C. R. & Variano, E. A. 2012 Shape effects on turbulent modulation by large nearly neutrally buoyant particles. *J. Fluid Mech.* **712**, 41–60.

Clift, R., Grace, J.R., Weber, M.E. & Weber, M.F. 1978 *Bubbles, Drops, and Particles*. Academic Press.

Csanady, G. T. 1963 Turbulent diffusion of heavy particles in the atmosphere. *J. Atmospheric Sci.* **20** (3), 201–208.

Elghobashi, S. & Truesdell, G. C. 1992 Direct simulation of particle dispersion in a decaying isotropic turbulence. *J. Fluid Mech.* **242**, 655–700.

Fröhlich, K., Schneiders, L., Meinke, M. & Schrder, W. 2018*a* Assessment of non-spherical point-particle models in LES using direct particle-fluid simulations. *AIAA Paper 2018-4714* .

Fröhlich, K., Schneiders, L., Meinke, M. & Schröder, W. 2018*b* Validation of lagrangian two-way coupled point-particle models in large-eddy simulations. *Flow Turb. and Combust.* **101** (2), 317–341.

Gao, H., Li, H. & Wang, L.-P. 2013 Lattice boltzmann simulation of turbulent flow laden with finite-size particles. *Comput. Meth. Appl.* **65** (2), 194–210.

Glowinski, R., Pan, T.W., Hesla, T.I., Joseph, D.D. & Periaux, J. 2001 A fictitious domain approach to the direct numerical simulation of incompressible viscous flow past moving rigid bodies: application to particulate flow. *J. Comput. Phys.* **169** (2), 363–426.

Jeffery, G. B. 1922 The motion of ellipsoidal particles immersed in a viscous fluid. *Proc. Royal Soc. Lond.* **102** (715), 161–179.

Lucci, F., Ferrante, A. & Elghobashi, S. 2010 Modulation of isotropic turbulence by particles of Taylor length-scale size. *J. Fluid Mech.* **650**, 5–55.

Ouchene, R., Khalij, M., Arcen, B. & Tanière, A. 2016 A new set of correlations of drag, lift and torque coefficients for non-spherical particles and large reynolds numbers. *Powder Technol.* **303**, 33–43.

Sanjeevi, S.K.P., Kuipers, J.A.M. & Padding, J. T. 2018 Drag, lift and torque correlations for non-spherical particles from stokes limit to high reynolds numbers. *Int. J. Multiphase Flow* **106**, 325–337.

Schneiders, L., Fröhlich, K., Meinke, M. & Schröder, W. 2019 The decay of isotropic turbulence carrying non-spherical finite-size particles. *J. Fluid Mech., under review* .

Schneiders, L., Grimmen, J. H., Meinke, M. & Schröder, W. 2015 An efficient numerical method for fully-resolved particle simulations on high-performance computers. *Proc. Appl. Math. Mech.* **15** (1), 495–496.

Schneiders, L., Günther, C., Meinke, M. & Schröder, W. 2016 An efficient conservative cut-cell method for rigid bodies interacting with viscous compressible flows. *J. Comput. Phys.* **311**, 62–86.

Schneiders, L., Meinke, M. & Schröder, W. 2017 Direct particle-fluid simulation of Kolmogorov-length-scale size particles in decaying isotropic turbulence. *J. Fluid Mech.* **819**, 188 – 227.

Shapiro, M. & Goldenberg, M. 1993 Deposition of glass fiber particles from turbulent air flow in a pipe. *J. of Aerosol Sci.* **24** (1), 65–87.

Shin, M. & Koch, D. L. 2005 Rotational and translational dispersion of fibres in isotropic turbulent flows. *J. Fluid Mech.* **540**, 143–173.

Squires, K. D. & Eaton, J. K. 1991 Measurements of particle dispersion obtained from direct numerical simulations of isotropic turbulence. *J. Fluid Mech.* **226**, 1–35.

Tennekes, H. & Lumley, J. L. 1972 *A first course in turbulence*. MIT press.

Voth, G. A. & Soldati, A. 2017 Anisotropic particles in turbulence. *Annu. Rev. Fluid Mech.* **49**, 249–276.